Mantle rain toward the Earth's surface: A model for the internal cycle of water

Denis Andrault, Nathalie Bolfan-Casanova

Mantle rain towards the Earth's surface: a model for the internal cycle of water

Denis Andrault [1,*] and Nathalie Bolfan-Casanova [1]

[1] Laboratoire Magmas et Volcans, CNRS-OPGC-IRD, Université Clermont Auvergne, France

* Correspondence to denis.andrault@uca.fr

Abstract

The internal or deep water cycle controls the volume of the oceans at the surface of the Earth. The advent of subduction 2-3 billion years ago initiated the transport of water back to the Earth's interior. With one ocean mass injected into the deep mantle over the last 2-3 billion years, some mantle regions must have become saturated and thus turned into a deep source of water. The mantle transition zone (MTZ) between 410 and 660 km depths is unlikely to be a source of hydrous melt, because its minerals can integrate several thousand ppm of water. On the contrary, the low-velocity layer (LVL) lying above the 410 km-discontinuity is one such source. As proposed by the "Transition-Zone-Water-Filter Model", the LVL is ubiquitously formed by the global uplift of the hydrous MTZ as a counter flow of subduction of slabs into deeper regions. The seismic signature of the LVL is compatible with the presence of 0.5 to 1% melt. This melt is produced by dehydration melting during upwelling of the mantle transition zone (MTZ) containing 2200(300) ppm wt H_2O, which corresponds to 0.6 ocean mass stored today in the MTZ. Hydrous silicate melt can be gravitationally stable just above the 410 km discontinuity. We propose, here, that at the upper limit of the LVL it becomes buoyant, especially where the mantle is particularly hot and/or hydrous. Once it becomes buoyant, the melt can percolate rapidly upwards through the mantle. As a consequence, the olivine-bearing mantle (OBM) could be almost saturated in water, due to the presence of upwelling hydrous melt. On its path, the melt may be responsible for the seismic low-velocity zones at mantle depths of between 80 and 150 km. It could also be a source for refertilisation of the lithospheric mantle. Based on this model, there should be ~1.0 oceanic mass (OM) stored in the upper mantle today. Secular cooling of the mantle implies an increased capacity of the OBM minerals to store water. The related decrease of oceans' mass at the Earth's surface is estimated to ~20% per one billion years.

Introduction

Water is present at the surface of our planet, which made the development of life possible. Cosmochemical arguments indicate that the amount of initial water in the planet could have been equivalent to several oceanic masses (1 OM = $1.4.10^{21}$ kg H_2O) depending on the source (Marty, 2012; Piani et al., 2020). Regardless of the origin of water on Earth, the deep water cycle determines how much of the accreted water resides at the surface and how much is trapped in the planet's interior. In this article, we develop a model based on the water storage capacity of mantle minerals, which brings new constraints on the distribution of water in the Earth's mantle.

Modern plate tectonics has been operating for the last 2-3 billion years (Ga), during which water has been continuously introduced into the mantle at subduction zones. This regassing flux is particularly difficult to assess, since the different layers of a slab have heterogeneous water contents and the degree of serpentinization can vary as a function of the geological setting. Recent estimates converge to 1 to 2 10^{12} kg.yr^{-1} of water transported to the mantle at subduction zones, which equates to 0.7 to 1.4 times the OM every Ga. Still, most of the water is thought to escape from the slab, percolate into the mantle wedge and trigger arc volcanism. Only 30% to 40% of the initial slab water could be efficiently carried down to the deep mantle, resulting in a flux of 0.3 to 0.8 10^{12} kg.yr^{-1} H_2O or 0.2 to 0.5 OM/Ga (Rupke et al.,

2004; van Keken et al., 2011). With increasing depth, the hydrous minerals that are stable at the Earth's surface break down upon heating and their water content can eventually be incorporated as H point defects in nominally anhydrous minerals (NAMs) (Ohtani et al., 2018; Padrón-Navarta and Hermann, 2017). This evolution is facilitated by an increasing H-solubility in NAMs with increasing pressure. At depths greater than 410 km, the formation of wadsleyite and ringwoodite increases hydrogen solubility by about one order of magnitude (Bolfan-Casanova et al., 2000; Ferot and Bolfan-Casanova, 2012; Inoue, 1994; Ohtani et al., 2000). We note that a high water storage capacity does not necessarily imply a high water content. Still, the discovery of the first terrestrial ringwoodite, which contains 1.2 wt% H_2O, in a deep diamond, is a proof that water can reach the transition zone (Pearson et al., 2014).

Today, there is no consensus on the water content in the mantle transition zone (MTZ) with budgets varying from 0.3 to 3 OM (corresponding to ~1000 ppm to 1 wt% H_2O). A number of arguments have been proposed for or against high water contents based on different approaches: (i) elasticity measurements related to observed velocity jumps at 410 km depth invoke water contents that vary between 0.3 and 0.6 wt% H_2O (Buchen et al., 2018; Mao et al., 2008). (ii) Electrical conductivity yields controversial results from negligible water contents (Yoshino et al., 2008) to 0.1-0.2 wt% (Huang et al., 2005). (iii) It has also been proposed that 1-2 wt% H_2O are necessary to explain the viscosity contrast at 660 km depth, as inferred from the effect of water content on dislocation mobility in bridgmanite and ringwoodite (Fei et al., 2017). Of course, the water content of the MTZ does not have to be homogeneous. Hydrogen has a slow diffusion rate in the solid state (Demouchy, 2010; Hae et al., 2006), which can, however, be counterbalanced by a long residence time of a slab in the MTZ (Fukao and Obayashi, 2013).

A crucial geological setting for the internal cycle of water is the global low velocity layer (LVL) above the 410 km discontinuity (Revenaugh and Sipkin, 1994; Tauzin et al., 2010; Vinnik and Farra, 2007). It is unanimously interpreted as being due to dehydration melting (Revenaugh and Jordan, 1991; Song et al., 2004; Tauzin et al., 2010) and this is a strong indication that the transition zone is hydrous. Melting triggered by dehydration of the rising mantle occurs if the water content in the MTZ exceeds the water solubility of the olivine-bearing mantle (OBM). The LVL displays an average shear-wave velocity drop ($\delta Vs/Vs$) of about 4-5%, as reported in previous works, compared to the overlying OBM. Based on the experimental relationship between the Vs drop in hydrous peridotites and the amount of melt produced, the melt content in the LVL was constrained between 0.5 to 1.0 vol. % (Freitas et al., 2017; Xiao et al., 2020). The Transition Zone Water Filter model (Bercovici and Karato, 2003) is used as a mean of explaining the presence and fate of the melt in the LVL. It involves a continuous production of melt in the LVL associated with a water cycle around the transition zone, functioning in a closed system with only one input: water from the slab. The hypothesis is that, once formed atop the 410 km discontinuity, the dense melt travels laterally in the LVL until it freezes in contact with the cold slab and gets subducted (e.g. (Leahy and Bercovici, 2007)). The water would be released again after crossing the 660 km boundary and would diffuse up to the MTZ because water incorporation in bridgmanite is low (Bolfan-Casanova et al., 2003; Liu et al., 2021). Seismic low velocity zones below the 660-km discontinuity indicate inefficient penetration of water into the lower mantle (Durand et al., 2017; Liu et al., 2016; Schmandt et al., 2014). However, it should be relatively difficult to subduct the LVL melt because it is lighter than the MTZ (Matsukage et al., 2005; Sakamaki et al., 2006). In addition, the sustainability of a closed deep water cycle with water entering from the slab is questionable: if 0.2 to 0.5 OM were to be injected into the deep mantle every Ga (see above), the water content in the MTZ should have increased by 0.4-1.5 OM and hence the ocean level decreased of the same amount since the beginning of plate tectonics 2-3 Ga ago. This is obviously too extreme and incompatible with previous proposals of a 10-20% decrease in ocean mass since the Archean, based on hydrogen isotopes (Lecuyer et al., 1998; Pope et al., 2012) and geodynamic modeling (Flament et al., 2013).

At the other end of the deep water cycle, mid-ocean ridges are the main recognized geological setting where water is transferred from the mantle to the crust (in this study, water outgassing by arc

96 volcanism is not considered in the mantle budget because we only consider the flux entering the mantle
97 beyond the formation of arcs, which is 0.3 to 0.8 10^{12} kg.yr^{-1} H_2O, as proposed by van Keken et al.,
98 2011). The rate of basalt production is ~20 km^3.yr^{-1} (Cogne and Humler, 2006), corresponding to ~1.2
99 10^{11} kg.yr^{-1} of water assuming 2000 ppm water in basalts (Michael, 1988). This is at least twice less
100 water than the lowest estimate of the water flux that is efficiently injected into the deep mantle by
101 subduction. The difference of at least 0.2-0.7 10^{12} kg H_2O.yr^{-1} points out to the need of considering other
102 possible sources of outgassing.

103   In this article, the strategy is to use quantitative constraints arising from mineral physics data, such
104 as the water storage capacity of minerals, the effect of partial melting on seismic properties, the effect
105 of composition (FeO and H_2O) on melt density, to develop a new model of the internal cycle of water.
106 We explain how the LVL can play a major role in extracting water from the major reservoir constituted
107 by the MTZ. The amount of water transported by the melt counterbalances the incoming water flow
108 associated with the entry of slabs into the MTZ, resulting in a stable water balance for the MTZ. We
109 investigate the conditions that can make buoyant a water-bearing melt formed in the LVL. Finally, we
110 describe the possible implications of such "mantle rain" and compare them with various geological
111 observations.

112

Maximum water solubility of the olivine-bearing mantle

114   The upper mantle is constituted of nominally anhydrous minerals (NAMs), which can
115 accommodate water in their lattice in the form of OH defects. The major upper mantle phase, olivine,
116 can incorporate more than 1000 ppm by weight of H_2O at high upper mantle pressures. The maximum
117 water solubility in olivine is a function of pressure, temperature and oxygen fugacity. When the
118 solubility limit is overpassed, an H_2O-rich phase appears, which can be a water-rich fluid at pressures
119 lower than a couple of GPa or a water-bearing silicate melt at higher pressures (Kessel et al., 2015; Mibe
120 et al., 2007). The phase equilibrium between the H_2O-bearing melt and the H-saturated olivine yields
121 the following relations:

122     $Mg_2SiO_4 + n\ H_2O <=> Mg_{1-n}H_{2n}SiO_4 + n\ MgO$ (1)
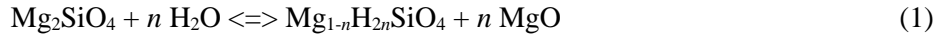
123     $[OH]^{olivine} = f_{H2O}{}^n \exp(\Delta G^{Ol}/RT)$ (2)

124   f_{H2O} is the water fugacity (see details in Suppl. Material) and ΔG^{Ol} (ΔH^{Ol} - TΔS^{Ol} - PΔV^{Ol}) the Gibbs
125 free energy of the formation of H-defects in olivine, n is the exponent describing the incorporation
126 mechanism. A best fit to the available experimental data (see (Ferot and Bolfan-Casanova, 2012) and
127 references therein) yields the following values (assuming that H is substituting for Mg, hence n=1): (i)
128 formation enthalpy ΔH^{Ol}= 47 kJ/mol, which compares well with previous reports of 37.1 kJ/mol (Bali
129 et al., 2008) and 50 kJ/mol (Zhao et al., 2004), (ii) formation entropy ΔS^{Ol} increasing from 75 to 92
130 J/molK when pressure increases from 1 to 12 GPa, as described in (Bali et al., 2008; Smyth et al., 2006),
131 and (iii) constant activation volume at ΔV^{Ol}=10.6 cm^3/mol (Kohlstedt et al., 1996; Mosenfelder et al.,
132 2006). Note that the hypothesis of site substitution of H in Mg (n=1) or Si (n=2) site is necessary to
133 extract the thermodynamic parameters from the solubility data, however, as demonstrated by (Yang,
134 2016) both sets of (n, ΔV) for n=1 or n=2 equally describe the data. Then, the maximum water-solubility
135 limit in olivine can be calculated at all P-T conditions relevant to the upper mantle using Suppl-Eq. 1
136 (Suppl. Material) addressing the value of f_{H2O} in Eq. 2.

137   We can also calculate the H-content in the other mantle minerals coexisting with olivine under
138 water-saturation conditions, using the published partitioning coefficients of H between olivine (Ol),
139 enstatite (Opx), clinopyroxene (Cpx) and garnet (Gt). We adopt a H partition coefficients of 1 between
140 olivine and garnet $D^{water}_{ol/gt}$ (Ardia et al., 2012; Novella et al., 2014), a $D^{water}_{opxx/ol}$ decreasing from 2 to
141 0.9 between Opx and olivine with increasing pressure from 2.5 to 9 GPa (Ferot and Bolfan-Casanova,

142 2012) and a $D^{water}_{cpx/opx}$ of 2 between Cpx and Opx (Demouchy et al., 2017). Finally, the well-known
143 modal fractions of each of these phases in a peridotite-type upper mantle (Irifune and Isshiki, 1998)
144 enables the calculation of the maximum water-solubility limit of the bulk olivine-bearing mantle (OBM)
145 at any depth, following a given adiabatic temperature gradient (Fig. 1).

146   For a present-day mantle potential temperature (T_P) of ~1650 K (Katsura et al., 2010), the H_2O
147 solubility limit of the OBM increases with depth from a few tens of ppm at the surface to ~1700 ppm
148 wt at the 410 km seismic discontinuity. The effect of temperature is major, with a solubility limit
149 decreasing by a factor of ~4 for T_P increasing from 1500 to 1950 K. It implies an increase of the water-
150 storage capacity of the mantle with secular cooling that we will discuss later in more detail (see also
151 (Dong et al., 2021)). We note that this calculation does not include possible effects associated with an
152 increased water solubility limit in the first 100 km of the lithosphere (Green et al., 2014; Mierdel et al.,
153 2007). In addition, the present model assumes conditions at which H_2O is the major hydrogen species
154 in the melt (Druzhbin et al., 2021).

Fig. 1: Water-saturation limit of a peridotite-type mantle. Colored curves present the water saturation limits of the mantle as a function of depth along an adiabatic temperature gradient prevailing for mantle potential temperatures (T_P) from (**A**) 1050 to 1400 K and (**B**) 1400 to 1950 K (derived from (Ferot and Bolfan-Casanova, 2012)). A hydrous melt (or fluid) occurs at water contents above the saturation limit. At a given mantle depth, the saturation limit first increases with temperature up to T_P ~1400K and then decreases with further T increase. The latter effect is due to silicate dissolution in the melt and, therefore, a decrease in the activity of water in the hydrous silicate-melt at high temperature (see (Bali et al., 2008) and text). Uncertainty in the determination of the water content using infrared is +/- 15% (Ferot and Bolfan-Casanova, 2012). Red dot corresponds to 1500 ppm H_2O in the mantle at 350 km depth (see text).

156
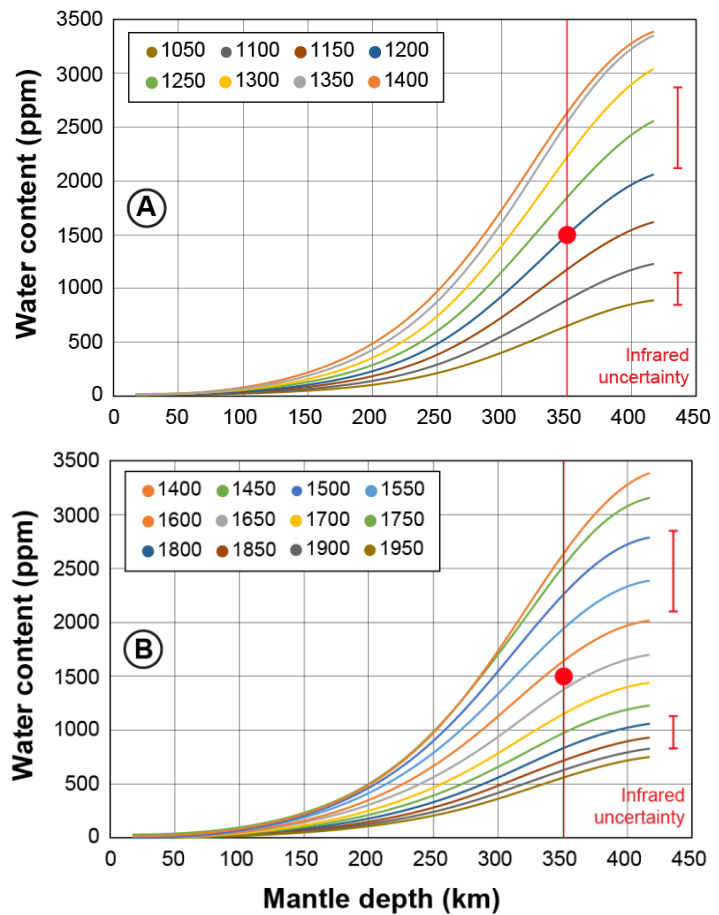
H_2O-saturated solidus of upper mantle

158   The solubility curves of Fig. 1 can be inverted into H_2O-saturated solidii (Fig. 2), considering that
159 a melt appears when, at any P-T condition above the second critical point of water, the water solubility
160 limit of the OBM is overpassed. The "500 ppm H_2O-saturated solidus", for instance, is the P-T profile
161 at which a water content above 500 ppm produces an incipient amount of melt saturated in H_2O. Due to
162 the formalism of Eq. 2 (see Suppl. Material), the calculated H_2O-saturated solidii present a complex
163 shape in the P-T diagram. In particular, they do not fall parallel to the dry-solidus (here we use that from

(Andrault et al., 2018), but the same observation would also stand for other works). Reasons for this are intrinsic to the thermodynamical properties of the minerals and hydrous melt. If we consider, for example, 1500 ppm of water in the mantle at 350 km depth (red dot in Fig. 1), such water content is higher than the water saturation limit, and would therefore yield the formation of a aqueous fluid, at temperatures below 1200 K (Fig. 1A) and hydrous melt above 1625 K (Fig. 1B). In contrast, the NAMs integrate 1500 ppm in the temperature range between 1200 and 1625 K. This yields a loop shape H_2O-saturated solidus in Fig. 2. We note that the effect of water on the thermodynamic parameters of the solid and melt may also induce mantle melting at temperatures just below the dry-solidus (Aubaud et al., 2004). In this case, however, neither the melt nor the solid residue would be saturated in H_2O. We do not report this effect in Fig. 2.
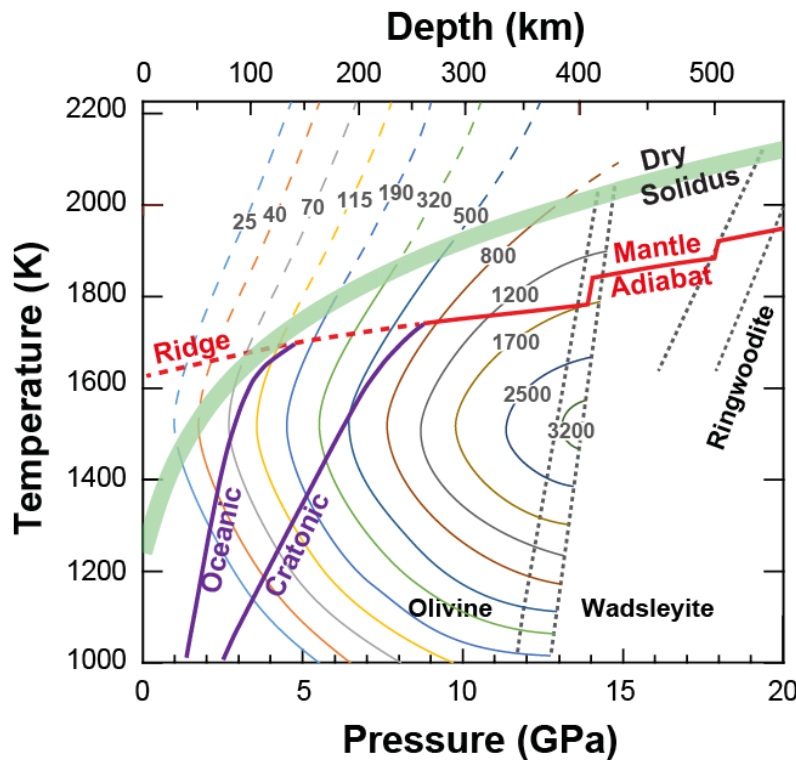

Fig. 2: The H_2O-saturated mantle solidii for water contents between 25 and 3200 ppm H_2O. The colored lines with associated water contents arise from the maximum water solubility displayed in Fig. 1. An H_2O-saturated melt appears on the left side of these curves (because water solubility decreases upon decompression) for H_2O-contents equal or superior to the reported number. We also report (i) the dry-solidus of chondritic-type mantle (green thick line (Andrault et al., 2018)) and (ii) the adiabatic temperature profile corresponding to T_P=1600-1650 K (Katsura et al., 2010). This figure does not consider the possible effect of a higher H_2O solubility limit in the lithosphere (Green et al., 2014; Mierdel et al., 2007; Sarafian et al., 2017). Uncertainty on water contents as in Fig. 1.

Continuous dehydration melting in the uprising mantle

A water content higher than the maximum water solubility induces the coexistence of water-saturated melt and solid residue. At a depth of 410 km, the OBM residue (produced by dehydration melting) should contain about 1700(200) ppm-wt H_2O (Fig. 2). This is much higher than the water content in the shallow source of mid ocean-ridge basalts (MORB), which contains between 50 and 250 ppm-wt H_2O at around 100 km depth (Michael, 1988). An appealing option to solve this discrepancy is that, during upwelling, the mantle H_2O-content decreases along with the water storage capacity limit (Ferot and Bolfan-Casanova, 2012) (Fig. 1). Hence, the mantle would remain partially molten at all depths (Hirschmann et al., 2005), until, at shallow depths, it finally reaches the value invoked for the MORB source. This seems incompatible with electrical conductivity measurements that do not favor a partially molten upper mantle between 180 and 350 km depth (Freitas et al., 2019; Toffelmier and Tyburczy, 2007). At least it implies that the fraction of melt should remain small. Based on the water-saturation profiles (Fig. 1), we calculate that the uprising by e.g. 10, 30 or 60 km from 410-km depth of the water-saturated mantle residue would produce ~0.07, ~0.25 or ~0.58 % of melt (colored dots in Fig. 3), respectively, assuming that the hydrous melt contains 6.5 wt% of water (see Table 1 and text below).

192 The same calculation can be performed for the uplift of the mantle residue from any mantle depth. The
193 maximum amount of melt produced by an uplift of e.g. 30 km is ~0.37 wt%. This calculation shows that
194 the amount of melt can be very small at any mantle depth if the melt that is regularly produced by
195 dehydration melting is rapidly segregated from the uprising mantle. For a comparison, the seismic and
196 electrical-conductivity anomalies observed between 80 and 150 km depth are compatible with more than
197 0.2% (Chantel et al., 2016) and between 0.3 to 2.0 wt% (Ni et al.,
198 2011) of melt, respectively. At intermediate upper-mantle depths,
199 the melt is buoyant and can travel upwards toward the Earth's
200 surface. This could make its presence undetectable to
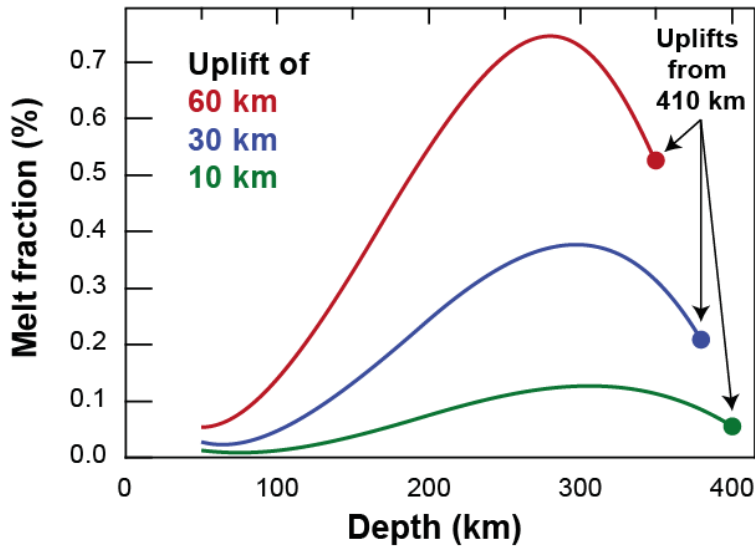201 geophysical measurements.

Fig. 3: **Dehydration melting in a rising upper mantle:** the uplift (i.e. adiabatic decompression) of a water-saturated residue induces continuous dehydration melting, due to a decrease of the water-saturation limit with decreasing mantle depth (Fig. 1). Here, we report the fraction of melt that can be expected at a given depth when a water-saturated mantle residue comes from 10, 30 or 60 km deeper, without loss of water during its ascent. Uplift from the 410 km seismic discontinuity are the colored dots. The curved shape with maxima around 275-300 km depth is due to the complex shape of the maximum water solubility limit in the mantle (Fig. 1). Uncertainties are +/- 15%, same as in Fig. 1.

202

Dehydration melting in the LVL: melt composition and phase diagram

204   The occurrence of a global low velocity layer (LVL) above the 410 km discontinuity (Revenaugh
205 and Sipkin, 1994; Tauzin et al., 2010; Vinnik and Farra, 2007) is unanimously interpreted as being due
206 to dehydration melting (Revenaugh and Jordan, 1991; Song et al., 2004; Tauzin et al., 2010). This is a
207 strong indication that the transition zone is hydrous. Melting triggered by dehydration of the rising
208 mantle occurs if the water content in the MTZ exceeds the water solubility of the olivine-bearing mantle
209 (OBM). The LVL displays an average shear-wave velocity drop ($\delta V_s/V_s$) between 4 and 5.6 %, as
210 reported in previous works, compared to the overlying OBM. Based on the experimental relationship
211 between the Vs drop in hydrous peridotite and the amount of melt produced, the melt content in the LVL
212 was constrained between 0.5 to 1.0 vol. % (Freitas et al., 2017; Xiao et al., 2020). Dihedral angles are
213 much lower (less than 10°) in the hydrous peridotite system at high-pressure (Freitas et al., 2017;
214 Yoshino et al., 2007) and the amount of melt necessary to explain $\delta V_s/V_s$ is predicted to decrease at
215 lower wetting angle (Hier-Majumder et al., 2014). Low wetting angles and low surface tension (Hier-
216 Majumder et al., 2006; Yoshino et al., 2007) favor the fast mobility of the melt at grain boundaries. This
217 is compatible with another major seismic observation in the LVL; no major melt ponds but instead a
218 continuous global layer of partial melt that is not limited to regions associated with subduction or mantle
219 plumes (Tauzin et al., 2010).

220   The composition of the water-bearing LVL-melt can be studied experimentally by reproducing an
221 equilibrium texture between peridotite and 0.5 to 1 wt% melt. Analyses of thin veins of melt
222 corresponding to ~2% partial melting indicate ~21.2 wt% FeO (recalculated after (Freitas et al., 2017)).
223 However, the composition of liquids originating from low degrees of partial melting can be biased by

crystallization upon quenching, inducing an enrichment of incompatible elements in the residual melt. Alternative methods have been developed in order to determine the composition of incipient melts accurately, such as the iterative sandwich method (Dasgupta and Hirschmann, 2007), which yields a melt FeO-content of ~13.4 wt% for the LVL melt (Condamine and Frost, 2018). On the other hand, density measurements show variations of +21 and -16.5 kg/m³ for every additional mol% FeO and wt% H_2O, respectively (Matsukage et al., 2005), in agreement with thermodynamical modeling (Freitas et al., 2017). As a result, a melt with an FeO-content of 11.6 wt% (used in (Matsukage et al., 2005)) or 13.4 wt% (ref. (Condamine and Frost, 2018), Table 1) would be neutrally buoyant at 350 km, at the top of the LVL, for H_2O contents of ~6 or ~7.1 wt% H_2O, respectively, in good agreement with previous work (Matsukage et al., 2005; Sakamaki et al., 2006). For modelling purposes, we use an average LVL-melt with reference FeO and H_2O contents of 12.5(1.0) and 6.5(1.0) wt %, respectively. We note that such FeO-content in the LVL of a peridotite-type mantle implies a solid-melt FeO partition coefficient D_{FeO}~0.65, which is compatible with D_{Fe}~0.56 proposed previously (Mibe et al., 2006).

| Composition of LVL melts		SiO2	TiO2	Al2O3	FeO	MgO	CaO	Na2O	H2O	Total
Matsukage et al. (2005)	meas. (wt%	35.5		3.3	11.6	30.4	14.1		6.0	100.9
	norm. (wt%	35.2		3.3	11.5	30.1	14.0		5.9	100.0
	mol%	27.8		1.5	7.6	35.5	11.8		15.7	100.0
Condamine and Frost (2018)	meas. (wt%	34.9	0.6	0.7	12.9	27.0	12.5	0.45	7.1	96.1
	norm. (wt%	36.3	0.6	0.7	13.4	28.1	13.0	0.47	7.4	100.0
	mol%	28.1	0.4	0.3	8.7	32.4	10.8	0.35	19.0	100.0
Freitas et al. (2017) F=2%	meas. (wt%	29.7		2.6	21.2	2.6	9.0	0.07	13.6	78.8
	norm. (wt%	37.8		3.2	27.0	3.3	11.4	0.09	17.3	100.0
	mol%	27.6		1.4	16.4	3.6	8.9	0.06	42.0	100.0
Preferred values	wt%				12.5				6.5	

Table 1: **Composition of the LVL melt**: (Matsukage et al., 2005) reported the neutral buoyancy in the LVL of a melt containing 11.6 wt% FeO and 6.0 wt% H_2O. The concentration in major elements of the LVL-melt was further refined using the iterative sandwich method (Condamine and Frost, 2018). They refined a melt Fe-content of ~13.4 wt%, which should be neutrally buoyant in the LVL for an H_2O content of ~7.1 wt% (Freitas et al., 2017; Matsukage et al., 2005). In a later work, incipient melting was induced by dehydration melting while measuring the sound wave velocities under conditions relevant to the LVL (Freitas et al., 2017). In these experiments, however, crystallization of some olivine could have occurred upon quenching, making the primary melt composition difficult to retrieve. We calculate a solid-melt FeO partitioning coefficient D_{FeO}~0.65 between the LVL melt and the solid mantle residue.

We now draw the melting diagram of the hydrous mantle at 14 GPa (Fig. 4A). The solidus is the water storage capacity based on mineral properties (Fig. 1). At temperatures of 1500, 1650 and 1800 K, the maximum H_2O-content in the mantle is 2800(300), 1700(200) and 1060(100) K, respectively. For a mantle potential temperature (T_P) of 1650 K, the hydrous melt that is in equilibrium with the water-saturated mantle should contain ~6.5 wt% H_2O (Table 1). Using mass conservation we calculate the melt fraction in the LVL as a function of the bulk water content (Fig. 4B). A bulk-mantle water content of 2200 ppm (left vertical dashed line), 0.5 or 1 wt% (middle vertical dashed line) leads to the formation of 0.75, 5.2 or 13 wt% of melt in the LVL. The latter values are well above the 0.5-1% of melt required to account for low LVL velocities (Freitas et al., 2017), clearly indicating that the bulk water content of the LVL, and that of the MTZ as well, must be well below 1 wt%. One may argue that higher MTZ water-content could be possible, if the LVL-melt returns quickly to the MTZ (Leahy and Bercovici, 2007). However, (i) the LVL-melt is lighter than the MTZ (Fig. 5), with therefore no reason to sink through the 410-km discontinuity, and (ii) return of hydrous LVL-melt into the MTZ would indefinitely increase its water content, which does not seem sustainable. A higher water content in the MTZ is only

251 possible if the water-content in the LVL-melt has been underestimated in previous studies (Table 1).
252 We will discuss the fate of the LVL-melt later in this article.

253   Finally, we draw the liquidus of this phase diagram passing through the melt composition at
254 T_P=1650 K (~6.5 wt%) and assuming that it has the same, but inversed, curvature than that of the solidus
255 (Fig. 5a). The resulting diagram suggests a slight decrease of the water content in the hydrous melt, from
256 e.g. 7.4 to 5.1, when the potential temperature increases from 1500 to 1800 K, respectively. This
257 indicates that for 2200 pm of water in the LVL, the melt fraction, Φ, increases from 0, ~0.75 and ~2.3
258 %, when temperature is 1500, 1650 and 1800 K, respectively.

Fig. 4: **(A) Phase diagram relevant to dehydration melting of the mantle**: above the 410 km depth discontinuity (~14 GPa), exceeding the maximum water storage capacity of peridotite induces dehydration melting. At a mantle potential temperature (T_P) of 1650 K, the solid mantle can store a maximum of ~1700 ppm H_2O (Fig. 1) and the melt contains ~6.5 wt% H_2O (Table 1). It results that a bulk water content of 2200 ppm (left vertical dashed line) leads to the formation of 0.75% of melt, in agreement with seismic observations of the low-velocity layer (Freitas et al., 2017). Thus, the melting diagram is mainly built using constraints from previous reports. Alternatively, a bulk water content of 1 wt% (middle vertical dashed line) would yield 13% melt. At T_P=1800 K, a bulk water content of 2200 ppm would produce 2.5% of melt containing 5.1 wt% H_2O. This diagram shows that mantle heterogeneities of temperature and water-content affect significantly the degree of partial melting and the melt composition. Uncertainty on water contents is same as in Fig. 1. **(B) Fraction of LVL-melt**: based on the solidus and liquidus profiles, we calculate, from Fig. 4A, the fraction of melt that must be present in the LVL based on bulk mantle water content and for T_P of 1500, 1650 and 1800 K. Inset is a zoom of the melt fraction at low water contents. Uncertainty on the melt fraction is estimated to ~25%.

259
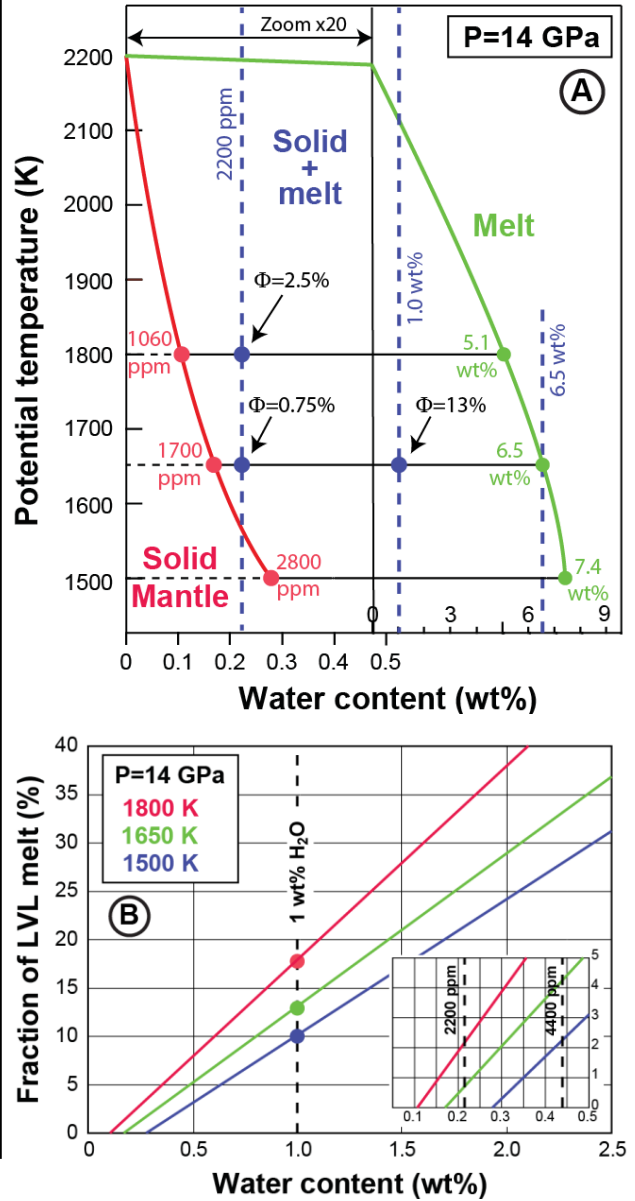
Melt-Mantle density contrast

261   The fate of the LVL-melt is primarily controlled by the melt-mantle density contrast ($\Delta\rho = \rho_{melt}$-
262 ρ_{mantle}). A melt-mantle density crossover (that is where both densities of solid and melt become equal),
263 occurs around the 410 km depth corresponding to ~14 GPa (Matsukage et al., 2005; Sakamaki et al.,
264 2006) (Fig. 5a), due to (i) the higher compressibility of the melt, compared to the solid mantle, (ii) the
265 absence of a major phase transition in mantle minerals above the 410 km discontinuity, and (iii) the

preference of FeO for the melt. Based on the equations of state and the dependence of the melt density on its FeO and H_2O contents (Jing and Karato, 2012; Matsukage et al., 2005), we recalculate the density contrast as a function of depth for various possible melt compositions (Fig. 5a). As expected, there is a maximum in the density contrast just above the 410 km discontinuity that then decreases with decreasing depth. In addition, we calculate that small variations in the FeO (+/- 3 wt%) and H_2O (+/- 2 wt%) contents can significantly affect the mantle depth at which neutral melt-mantle buoyancy is achieved.
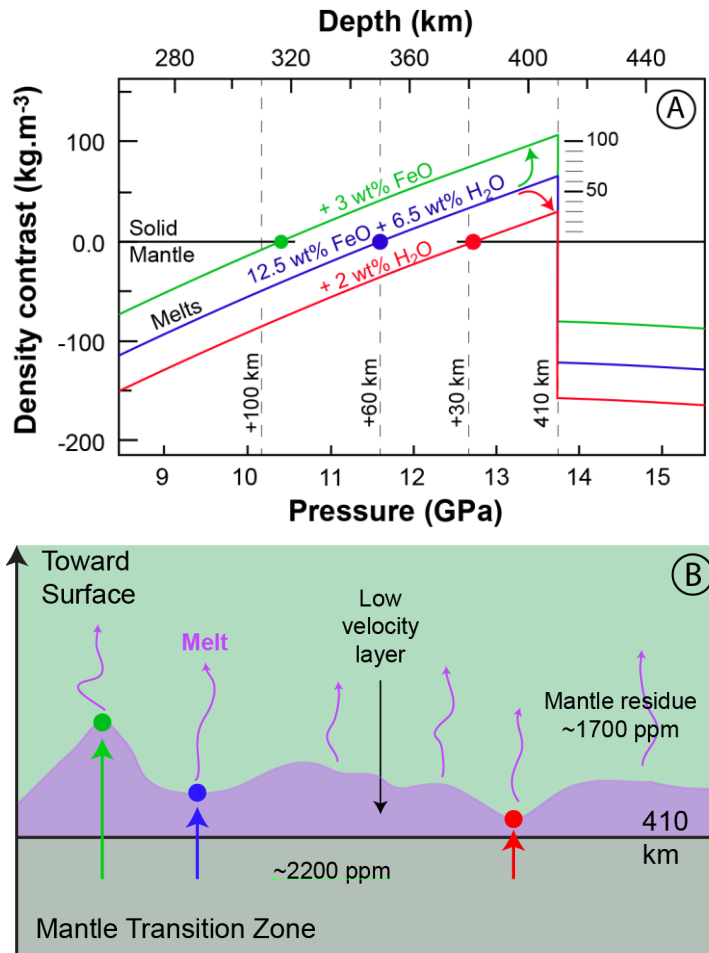

Fig. 5: (A) Melt-Mantle density cross-over. Because melts have a higher compressibility compared to the solid mantle, the density difference between melt and solid increases with increasing depth, and the melt eventually becomes denser than the solid between the neutral buoyancy depth and the 410 km depth, at the olivine-wadsleyite phase transition. This depth interval (ΔZ_{LVL}) defines the thickness of the LVL. Neutral melt-mantle buoyancy is expected at the upper limit of the LVL, which is seismically observed 60 km in average above the 410 km discontinuity (blue dot). For a mantle of peridotite composition, the LVL-melt should contain 12.5 wt% FeO and 6.5 wt% H_2O (blue line, Table 1). The melt density changes significantly as a function of its FeO (green line) and H_2O (red line) contents (Matsukage et al., 2005; Sakamaki et al., 2006). Thus, the thickness of the region where the melt is denser (within ΔZ_{LVL}), can vary laterally inside the mantle due to heterogeneities in temperature and composition (see text). Depending on their composition, melts can be buoyant (less dense) at depths shallower than the green, blue or red dot. For comparison, density of the OBM at 410 km depth is ~3500 kg.m^{-3}. Uncertainties are detailed in previous works (Matsukage et al., 2005; Sakamaki et al., 2006) **(B) The "mantle-rain" model** proposes that the LVL-melts rise upward through the mantle once they reach the upper limit of the LVL. Melts migration occurs vertically and laterally along grain boundaries. The observed regional variations of the LVL-thickness can be explained by mantle heterogeneities in FeO, H_2O contents and temperature, which induce LVL-melts that are relatively denser (green dot) or lighter (red dot), compared to the typical LVL-melt (blue dot, Table 1). Still, any melt composition becomes buoyant above a given mantle depths (Fig. 5a).

Thus, variations in melt composition can create variations of the thickness of the LVL (ΔZ_{LVL}). Indeed, the top of the LVL is the point of neutral melt-mantle density (red, blue and green dots in Fig. 5a) and further uprising of the mantle beyond this limit yields a buoyant melt, which upward migration is forced by gravity. A melt composition enriched in iron, by e.g. 3 wt%, yields a denser melt that is gravitationally stable across a broader region (from 410 to ~320 km depth, up to the green dot in Fig. 5a), thus implying an LVL which is thicker, by e.g. +40 km, compared to the mean mantle, which melt is gravitationally stable up to ~60 km above the 410 discontinuity (blue dot in Fig. 5a). In

9

contrast, a melt enriched in H_2O, by e.g. 2 wt%, yields a lighter melt that is gravitationally stable up to 30 km only above the 410 km discontinuity (red dot in Fig. 5a). Chemical variations of the melt can be induced by mantle heterogeneities in temperature, water content or even fertility. They can induce variations of the LVL thickness from ~30 to ~100 km that are compatible with seismological observations (Revenaugh and Sipkin, 1994; Tauzin et al., 2010; Vinnik and Farra, 2007).

Knowing the melting diagram of hydrous peridotite (Fig.4a), the manner in which the variation in mantle composition and temperature affect the density of the LVL melt can be assessed by constraining the melt fraction (Fig.4b). Indeed, given that the 410 km discontinuity is well explained globally by a peridotite (or pyrolite) mantle, there is no reason at this stage to invoke other components such as eclogite or sediments.

(i) Since water is an incompatible compound, a local increase of the water content in the MTZ would induce a higher degree of partial melting in the LVL (Fig. 4b). We determine that twice more water in the MTZ than the value of 2200 ppm would produce ~6 times more LVL-melt (~4.4 wt%, see inset of Fig. 4b). Such melt would contain the same amount of H_2O (fixed at the liquidus, Fig. 4a), but a lower FeO-content (reduced by ~1% compared to 6.5 wt%; Table 1), according to mass conservation $[FeO]_{Melt}=[FeO]_{Mantle}/(\Phi+(1-\Phi)D_{FeO})$, where Φ is the melt fraction and using D_{FeO}~0.65, the solid-melt FeO partition coefficient. As a result, such melt would be ~0.2% lighter (+21 kg/m^3 for every additional mol% FeO (Matsukage et al., 2005)), compared to the melt formed from a mantle containing 2200 ppm H_2O. Similarly, a bulk 1 wt% H_2O would produce 13 wt% of LVL-melt (see Fig. 4b) with ~5% less FeO and a density lowered by ~1%. The mantle residue also loses some Fe with increasing Φ, however, to a much lesser extent. Altogether, bulk water contents of 4400 ppm or 1 wt% imply a decrease of ~6.3 and ~36 kg.m^{-3}, respectively, from a melt-mantle density contrast of ~65 kg.m^{-3} at the base of the LVL for a water content of 2200 ppm H_2O (Fig 5a). This would yield a LVL up to ~30 km thinner, compared to the average mantle.

(ii) The mantle could also present variations in its fertility, implying significant heterogeneities in FeO-content, which incompatibility and molecular weight have important consequences on melt density, as we have seen. A reduction by 10% (from e.g. 8.0 to 7.2 wt% FeO) in the FeO content of the mantle would result in a stronger decrease of the melt FeO content, compared to that of the residue (due to $D_{Fe}^{Solid/Melt}$=0.65), and a decrease of the melt-mantle density contrast by 0.8% or ~28 kg.m^{-3} (Matsukage et al., 2005). This would yield a LVL ~30 km thicker, compared to the average mantle.

(iii) A locally higher mantle temperature would increase Φ (Fig. 4b). Such LVL-melt would be depleted in both H_2O and FeO, compared to mean mantle conditions as incompatible elements get diluted with increasing melt fraction. It is difficult to tell which of the two opposite effects (increasing FeO content or increasing H_2O content) dominates the melt-mantle density contrast. The imprecise shape of the liquidus in Fig. 4a yields a large uncertainty on Φ as a function of temperature. However, the effect of bulk water content could be significant, as illustrated by the change from 0.75 to 2.5 wt% of melt when T_P increases from 1650 to 1800 K, for a bulk H_2O-content of 2200 ppm (Fig. 4b).

(iv) Finally, the presence of carbonate in the LVL melt cannot be discarded. Carbonates are subducted to great depths and are known to react to form diamond in the transition zone (Pearson et al., 2014; Shirey et al., 2021). If present in the melt, C in the form of CO_3^{2-} is expected to increase the melt buoyancy relative to the surrounding mantle. Still, carbonates may more likely be present at depths shallower than ~150 km where the oxygen fugacity is higher (Stagno et al., 2013).

Overall, mantle heterogeneities in FeO and H_2O contents and possibly also temperature and CO_2-content appear to have a significant effect on the melt buoyancy, especially in the shallow part of the LVL where the melt-mantle density contrast is small (Fig. 5a). We acknowledge important uncertainties in the amplitude of the melt-density dependence on FeO, H_2O, CO_2 contents and temperature. However,

335 the trends described above are qualitatively correct and, therefore, mantle heterogeneities could be a
336 major controlling parameter of the LVL-thickness.

337
Fate of hydrous-melt in the upper mantle

339   Overall, we expect the production of water-rich melts to be widespread in the OBM: not only the
340 LVL could be a continuous source of buoyant melts, but the uprising residual mantle is expected to
341 dehydrate progressively on its way toward the surface (Fig. 3). While the vertical mobility of the melt
342 is certainly triggered by a melt being more buoyant with increasing elevation from the 410 km
343 discontinuity (Fig. 5a), lateral migration is also facilitated by several parameters: (i) a low dihedral angle
344 in the hydrous peridotite system at high pressure (Yoshino et al., 2007) (ii) significant grain to grain
345 surface energy between silicate minerals, ~4 J/m^2 for olivine (Swain and Atkinson, 1978), though
346 unfortunately poorly constrained in the presence of majoritic garnet, the second major phase at high
347 upper-mantle depths and (iii) a major relaxation of the surface energy under hydrous conditions (de
348 Leeuw et al., 2000). Large-distance melt propagation has already been proposed for the LVL-melt above
349 the 410 km discontinuity (Leahy and Bercovici, 2007). Widespread circulation of metasomatic agents
350 is also recognized in the cratonic lithosphere (O'Reilly and Griffin, 2013). We argue that a similar
351 process also occurs within the convecting mantle and it is possible that chemical reactions favor mantle
352 refertilization. As observed in nature, the percolation of hydrous melt into a mantle region that is not
353 saturated in water would induce hydration of NAMs, drying out the melt and inducting its solidification
354 (Denis et al., 2015; Doucet et al., 2014; Le Roux et al., 2007). Over geological time, the travelling melts
355 can resolve at least partially the heterogeneity in water content between the different mantle regions. In
356 this way, all mantle regions (even those that do not undergo dehydration melting upon uprising) could
357 achieve a water content close to the saturation limit. For further modeling of the total water content in
358 the upper mantle, we consider that the minerals of the OBM carry an amount of water that is close to
359 the water saturation limit (Fig. 1).

360   On its way through the OBM, the buoyant hydrous melt eventually meets a critical depth where it
361 decomposes into a mixture of volatile-bearing fluid and silicate-melt (Kessel et al., 2015; Mibe et al.,
362 2007). The appearance of a fluid (Gaillard et al., 2008; Hirschmann, 2010) as well as the local
363 accumulation of a viscous silicate-melt (Chantel et al., 2016; Priestley and McKenzie, 2013) could
364 produce the low velocity zones (LVZ) detected by seismic and electrical conductivity measurements.
365 The range of depths between 80 and 150 km where LVZs are detected (e.g. (Debayle and Ricard, 2012;
366 Kawakatsu et al., 2009)) is compatible with the P-T conditions, around 3.8 GPa and 1273 K, at which
367 the second critical end point was reported in the peridotite-H_2O system (Mibe et al., 2007). It is therefore
368 appealing to make a causal link between the "mantle rain" and the LVZs. A major observation that needs
369 to be taken into account is that the LVZ seismic and electrical-conductivity anomalies become weaker
370 and deeper with increasing plate age (e.g. (Debayle et al., 2020)), while we expect ubiquitous upwelling
371 of the melt from the LVL. A greater impact of the melt in young geological settings could arise from
372 two major factors: (i) less hydrous melt reaches old compared to young lithospheres. The mantle
373 underneath mid-ocean ridges is uprising and, therefore, the mantle residue is expected to undergo
374 continuous dehydration melting on its path (Fig. 3). The hydrous-melt produced this way is added to the
375 melt coming from the LVL (left side of Fig. 6). Alternatively, the mantle underneath an old lithosphere
376 should be either stagnant (in depth) or sinking. Thus, no melt is produced by dehydration-melting upon
377 decompression. Now if we consider that the regions where the mantle is sinking, one can expect that it
378 would react and stop the LVL-melt at mid upper-mantle depth due to mantle rehydration (right side of
379 Fig. 6). (ii) Young oceanic crust presents a much steeper temperature gradient in the first 100-150 km
380 depth, compared to the continental crust. By comparing these temperature profiles and the mantle
381 solidus, it appears that the formation of a water-saturated melt evolves progressively from ~150 ppm at

382   100-150 km depth, to ~700 ppm H_2O at 250-300 km depth, for young oceanic to old continental settings,
383   respectively (Fig. 2). This denotes a larger impact of water in the young lithosphere.
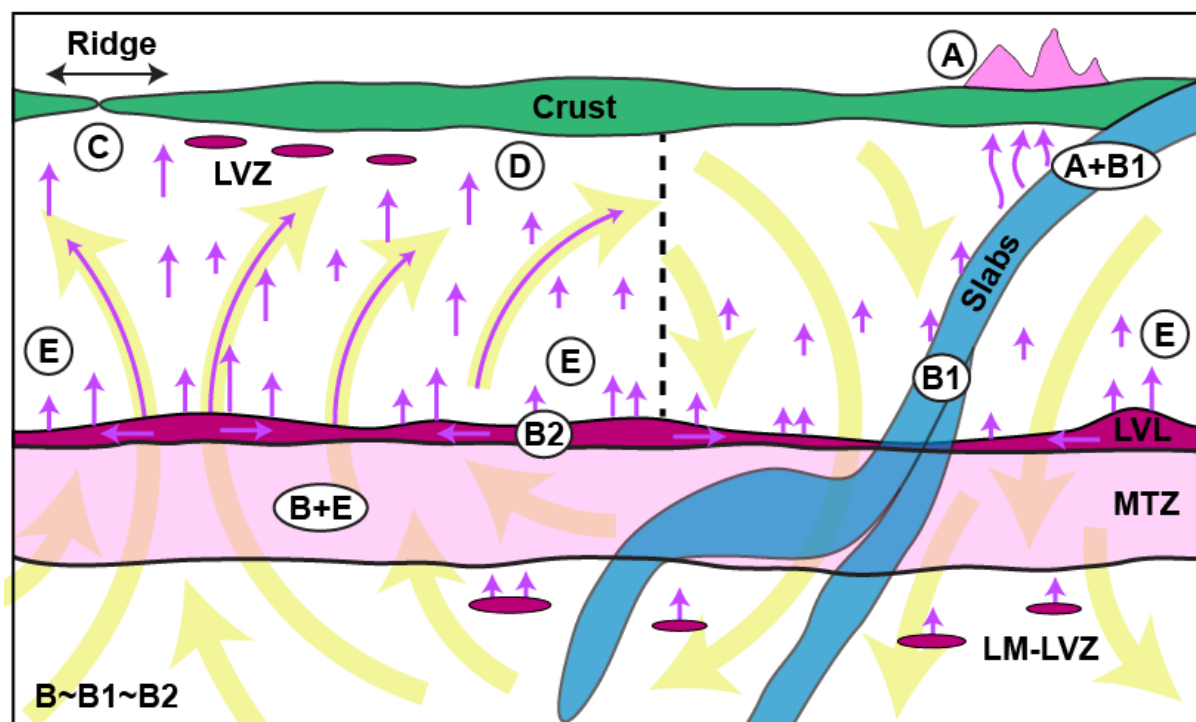

Fig. 6: Internal cycle of water and the mantle rain model. The mantle convects upward or downward in left and right parts of the diagram, respectively. Upward movement should dominate, though, in order to balance the inflow of slab (blue) into the deep mantle. Upon uprising of the water-rich MTZ material (light pink) and crossing of the 410 km mineralogical discontinuity, the mantle becomes water-saturated and dehydration melting produces the LVL-melt (dark pink layer). In addition, the uprising of the mantle residue continuously produces a water-bearing melt (curved pink arrows, Fig. 3). Above the upper limit of the LVL, the melt is buoyant and rises toward the surface (linear pink arrows, Fig. 5). Migration of the hydrous melt should take place in all directions, due to low surface tension; for clarity, lateral melt movements are not represented in this figure, except in the LVL. In mantle regions that are sinking, chemical reactions with the travelling hydrous melt is expected to hydrate mantle NAMs. Similar reactions occurring in the lithospheric mantle (point D) can produce mantle refertilisation and eventually intraplate volcanism. (A+B1) is the inflow of water at subduction zones; ~1-2 10^{12} kg.yr^{-1} but only (B1) penetrates the deep mantle; 0.3-0.8 10^{12} kg.yr^{-1}. (B2) is the water contribution to produce the LVL-melt: 0.5(0.2) 10^{12} kg.yr^{-1}. (C) is the outflow of water at the ocean ridges; ~0.1 10^{12} kg.yr^{-1}. (B2) should roughly equal (C+D), with (D) the water flux into the lithosphere: 0.2-0.7 10^{12} kg.yr^{-1}. While (A) to (D) are water fluxes, (E) is the steady water content in the solid upper mantle. Considering that the upper mantle is almost saturated in water yields a total water content of 8.5(0.8) 10^{20} kg H_2O or 0.6(0.1) mass of the oceans. Calculations are detailed in the main text and captions of other figures. This cycle assumes a constant amount of water in the lower mantle and in the core. We note that some dehydration melting may occur below the 660 km and induce low seismic-velocity zones (LM-LVZ).

384   The transfer of melts and fluids enriched in incompatible and volatile elements to the lithospheric
385   mantle may contribute to its refertilisation. In addition to well identified, hydrous metasomatism in
386   mantle xenoliths from the cratonic mantle (Doucet et al., 2014; Le Roux et al., 2007), the presence of a
387   few percent of pyroxenite is often invoked to explain the trace element and isotopic composition of mid-
388   ocean ridge basalts (MORBs) originating from the oceanic mantle (Lambart et al., 2009). The hydrous
389   melts originating from the transition zone could also help explaining the occurrence of less well-known
390   magmatism. For example, the presence of residual fluids under-plating the crust could trigger the

391 formation of petit-spot volcanoes (Machida et al., 2017). Hydrous plumes coming from the MTZ have
392 also recently been invoked to explain continental magmatism such as continental flood basalts beneath
393 China (Kuritani et al., 2019; Wang et al., 2015), and beneath the Turkish-Iranian plateau
394 (Soltanmohammadi et al., 2018). It is also notable that only a few identified mantle plumes (Liu et al.,
395 2018; Vinnik and Farra, 2007; Zhang et al., 2018) come from great depth (Courtillot et al., 2003).

396

Water budget in the present-day deep mantle

398 In mantle regions subjected to continuous upwelling, melt is continuously formed in the LVL, while
399 a partially depleted, but still water saturated, residue proceeds upwards (Bercovici and Karato, 2003).
400 On a global scale, an incoming flow of ~2.5 10^{11} $m^3.yr^{-1}$ of subducted slab material (Wen and Anderson,
401 1995) through the MTZ implies an average uplift of ~0.6 $mm.yr^{-1}$ across the whole 410 km discontinuity.
402 In order to induce dehydration melting, the water content in the transition zone needs to be higher than
403 the maximum storage capacity of the OBM, which is 1700(200) ppm H_2O at 410 km for a mantle
404 potential temperature of 1650 K (Fig. 1, see details in Suppl. Material). In addition, some water is carried
405 by 0.5 to 1% of LVL melt containing 6.5(1) wt% H_2O. This represents an additional 300 to 700 ppm
406 (thus, 500(200) ppm) H_2O, yielding a total mantle content of 2200(300) ppm H_2O (Fig. 4) to explain the
407 seismic velocity drop in the LVL. We now consider that the average water content in the MTZ is
408 comparable to that in the LVL (2200(300) ppm), which is only ~30% higher than the maximum
409 solubility limit of the mantle (1700(200) ppm) in the LVL. This assumption implies that there is no
410 accumulation of melt in the LVL, but instead continuous melt formation by dehydration melting and
411 escape by *Mantle Rain* of a same amount of LVL-melt. Here, we evaluate what are the consequences of
412 this assumption: (i) if the water content of the mantle uprising from the MTZ would be lower, between
413 1700(200) and 2200(300) ppm water, then there would still be dehydration melting. There would be less
414 LVL-melt produced for a same amount of uprising MTZ material. This would lower the fluxes of LVL-
415 melt out of the LVL and loss by uprising. (ii) Alternatively, more than 2200(300) ppm water in the MTZ
416 would produce a fraction of LVL-melt higher than expected from the comparison between experiments
417 and seismic data. This could be accommodated by the *Mantle Rain* model with a greater flux of uprising
418 LVL-melt. Still, it should be compensated by a higher influx of water in the MTZ, which does not seem
419 to be available (see text above and Fig. 6). It makes it unreasonable a MTZ water content significantly
420 higher than 2200(300) ppm. In summary, slight variations of the MTZ water content away from the
421 average value of 2200(300) ppm does not significantly change either the *Mantle Rain* model or the upper
422 mantle water balance estimate that we develop below. We note that this value is far below the level of
423 water saturation in MTZ, because wadsleyite can include up to 5 times more hydrogen than olivine at
424 these P-T conditions (Ferot and Bolfan-Casanova, 2012). Based on the average value of 2200(300) ppm,
425 the MTZ should contain 8.5(0.8) 10^{20} kg of water, corresponding to 0.6(0.1) OM.

426 The continuous rise of the water-bearing MTZ material by ~0.6 $mm.yr^{-1}$ corresponds to a total of
427 ~2.0(0.3) 10^{12} $kg.yr^{-1}$ H_2O crossing upwards the 410 km discontinuity. This value is significantly larger
428 than the 0.3 to 0.8 10^{12} $kg.yr^{-1}$ H_2O injected in the deep mantle by subduction ((van Keken et al., 2011);
429 B1 in Fig. 6). Instead, it is the flux of water producing the LVL-melt, about 0.5(0.2) 10^{12} $kg.yr^{-1}$ (B2 in
430 Fig. 6), that is well compatible with the flux of water entering the MTZ by subduction. This indicates
431 that the production of LVL-melt is primarily triggered by the amount of deeply subducted water. On the
432 other hand, the origin of the water present in NAMs uprising to the LVL cannot come from the subducted
433 water. In the framework of global convection, NAMs are expected to cross the 410 km boundary in both
434 directions and, for this reason, their contribution to the water transfer through the 410 km boundary is
435 balanced. By analogy, the situation is comparable to the presence of incompatible elements in peridotite;
436 they do not come from the subduction of MORBs. The water content of NAMs sinking through the 410
437 km discontinuity is unknown. However, it could be close to the NAMs saturation limit due to reaction
438 with hydrous-melt present in the upper mantle (see above). In addition, they cross the water-saturated

439 LVL and could react there with the water-bearing melt. For this reason, we consider that the water
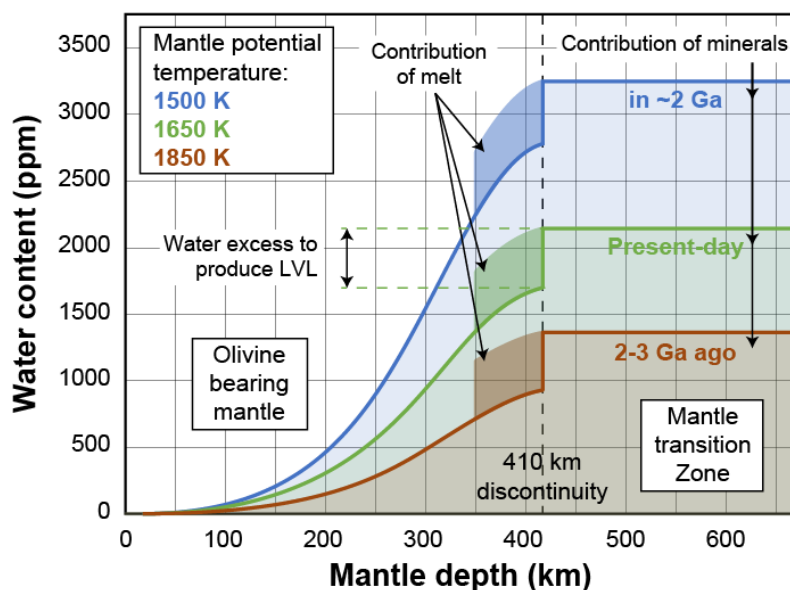440 content of NAMs in the upper mantle as a constant (contribution E in Fig. 6).

Fig. 7: Water content in the upper mantle as a function of mantle potential temperature. At a depth shallower than 410 km, the H_2O content of the mantle follows the water-saturation profiles (Fig. 1). On the other hand, the water content in the mantle transition zone can be estimated as being the sum of the solubility limit in the mantle above 410 km and the water content needed to produce 0.5 to 1 wt% of hydrous-melt in the low-velocity layer, in agreement with seismic data. The mean thickness of the LVL is ~60 km, but depends on mantle heterogeneities in H_2O and FeO contents, and temperature (see text). The same calculation is performed for mantle potential temperatures of 1850 K (red: 2-3 Ga ago), 1650 K (green: ~present-day) and 1500 K (blue: in the future). Uncertainty on water contents is same as in Fig. 1.

441 Now we calculate the total amount of water present in the
442 upper mantle (Fig. 7). An OBM close to its water saturation limit
443 yields an integrated value of its water content of ~4.3(0.4) 10^{20} kg
444 or ~0.31(0.03) OM. Added to the 0.6(0.1) OM in the MTZ (see
445 above), we conclude that a water-equivalent of ~1.0(0.1) OM of
446 water currently resides in the mantle above the 660 km
447 discontinuity. We acknowledge that this calculation does not
448 include possible effects associated with an increase in the water
449 solubility limit in the lithospheric mantle and the crust (Green et al.,
450 2014; Mierdel et al., 2007; Sarafian et al., 2017). For estimating a
451 water budget over the entire mantle, the amount of water residing
452 in the lower mantle should also be considered: different
453 experimental works based on high-quality single-crystal of
454 bridgmanite find a radically different water storage capacity from ~100 ppm (Bolfan-Casanova et al.,
455 2003) to ~1000 ppm (Fu et al., 2019), which translates into maxima of ~0.3 to ~3 OM in the lower
456 mantle. Ferropericlase and $CaSiO_3$-perovskite may also integrate minor amounts of H. In addition, some
457 water may be carried below the 660 km discontinuity in dense hydrous phases that remain stable in low-
458 temperature slabs (Nishi et al., 2014; Pamato et al., 2015). Still, partition coefficients greater than 10
459 between most NAMs and bridgmanite favor the storage of water in the MTZ, compared to the lower
460 mantle (Bolfan-Casanova et al., 2003) and thus we consider that the lower mantle should be fairly dry.

461

Water budget of the mantle over the Earth's history

463 We evaluate the amount of water that has been stored in the mantle over the course of the Earth's
464 history. Analyses of ancient non-arc basalts and komatiites suggest a rate of mantle cooling of ~100
465 K/Ga (e.g. (Herzberg et al., 2010)). A higher mantle temperature in the past implies a lower water storage
466 capacity for NAMs (Fig. 1) and thus less water stored in the upper mantle (Fig. 7). The amount of water
467 stored in the MTZ in the past can be estimated from the maximum water storage capacity of the mantle
468 just above the 410 km discontinuity making following assumptions: (i) the LVL has persisted since the
469 establishment of slab subduction, due to the parental link between subducted water and formation of the
470 LVL (see above). (ii) LVL properties, e.g. its dependence on mantle temperature and water content,

have remained the same over time, which enables the use of the melting diagram (Fig. 4). It implies that the excess water in the MTZ, compared to the OBM, is regulated by the LVL (Fig. 7). In other words, we assume that although the deep water cycle has evolved over the last 2-3 Ga, a stable equilibrium between the flow of water into the MTZ via subduction and the flow of water out the MTZ via melt formed at the LVL was established early on and maintained over geological times. We thus obtain water contents of 930(100) or 2800(300) ppm for the OBM at 410 km depth from Fig. 1, and 1400(200) or 3300(500) ppm for the MTZ, for T_P varying from the highest values of 1850 K (in the past) to 1500 K (in the future), respectively (Fig. 7).

The water storage capacity in the entire upper mantle (above 660 km depth) is found to increase from ~0.6(0.1) to ~1.4(0.2) OM from 2-3 Ga ago (T_P ~1850 K) to a point in the future when T_P will achieve 1500 K (Fig. 8). This corresponds to a net decrease of the water elevation of the oceans by ~900 m in the last 2-3 Ga, for a mean elevation today of 4.5 km. These trends correspond to a decrease of the oceanic mass of ~20% per Ga, in agreement with previous findings of a loss of several 10s % of the OM over geological time, based on hydrogen isotopes (Lecuyer et al., 1998; Pope et al., 2012) and geodynamic modeling (Flament et al., 2013). The mantle storage capacity will continue to increase to a maximum value of ~1.6 OM, when T_P may eventually decrease to 1400 K in several Ga from now.
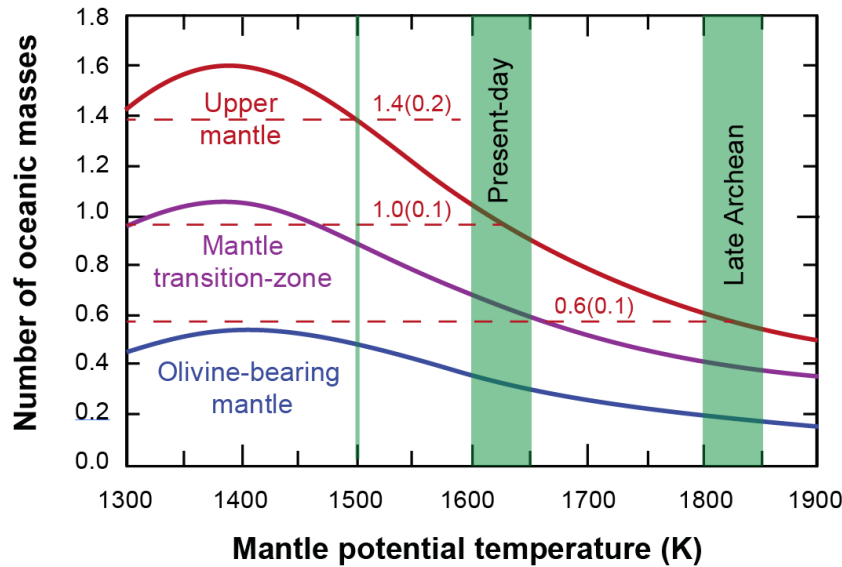
Fig. 8: **Water content of upper mantle reservoirs throughout Earth's history**. Water contents in the entire upper mantle (red), constituted of the OBM (blue) and of the MTZ (purple), calculated from the integration of water contents as a function of depth (Fig. 7) for various T_P. With present-day T_P ~1650 K, we expect ~1.0(0.1) ocean mass (OM) trapped in the mantle above 660 km (central red dashed line), with ~0.4 and ~0.6 OM in OBM and MTZ, respectively). The water storage capacity in the upper mantle increases with secular cooling at a rate of ~20% of the ocean mass per billion years. Uncertainty is +/-15% similar to that of Fig. 1.

Finally, we investigate the critical amount of water needed to produce a planet like the Earth in terms of the surface ratio between oceans and emerged-continents. For the Earth, the present-day ~2.0 OM (1.0 OM residing at the surface and 1.0 OM in the mantle) stored above the 660 km discontinuity ensures the existence of an ocean at the surface of the planet regardless of its age (i.e. its mantle temperature). During the Archean, the mantle was hotter and thus its water storage capacity was lower, ~0.6 OM, implying a volume of Archean oceans ~1.3 times that of today's. This agrees with inferences, based on the $^{87}Sr/^{86}Sr$ isotopic composition of marine carbonates, that there was little (less than 4%) emerged land 2.5 Ga ago (Flament et al., 2008). With cooling to the present-day potential temperature of 1650 K, the hydrosphere would have been entirely buried into the solid mantle if the total terrestrial water content had been less than ~1.0 OM (Fig. 8). In the future, the water storage capacity of the upper mantle is expected to further increase with secular cooling, possibly reaching a maximum of ~1.6 OM for a mantle potential temperature of 1400 K. This would leave only 0.4 OM at the Earth's surface. Therefore, variations of the total amount of water in the mantle of a planet with the size of the Earth

504 may easily result in no emerged land early in the history, or the absence of a surface ocean a few Ga
505 after the planet's formation, just because of the interplay with the mantle.

506

Conclusion

508   In this article, we develop the "mantle rain" model and its implications. The model is based on the
509 mechanism of dehydration melting taking place above the 410 km discontinuity and producing a water-
510 saturated melt and solid residue, which together form the LVL observed by seismology. Starting from
511 the well-accepted concept of a neutral melt-mantle buoyancy at the upper limit of the LVL, we develop
512 the idea that the LVL is a source for upwelling melts. With such mechanism, it becomes possible to
513 balance the incoming (by subduction) and outgoing (by rise of LVL-melt) water flows for the MTZ.
514 Within the upper mantle, a water-bearing melt is expected to travel several orders of magnitude faster
515 than the mantle residue stirred by convection movements. The melt could travel relatively fast laterally
516 and vertically, favoring homogenization of the water content, mantle refertilisation, seismic anomalies
517 such as the LVZ, intraplate volcanism, etc.
518   The occurrence of dehydration melting in the LVL also offers a clue to estimate the average water
519 content in the MTZ. It should be higher than the maximum water-storage capacity of the OBM at 410
520 km depth, 1700(200) ppm, as determined experimentally, and should also account for the continuous
521 production of the water-bearing LVL-melt: thus, it should be ~2200(300) ppm H_2O for Tp of 1650 K.
522 Based on this value and with the idea that the OBM should be almost saturated in water, we find that ~1
523 ocean mass of water is stored in the entire upper mantle today. The same calculation can be performed
524 for mantle potential temperatures higher (in the past) and lower (in the future) than that of 1600-1650 K
525 prevailing today. With an increasing water storage capacity of the mantle as a function of decreasing
526 mantle temperature, the mass of the oceans at the Earth's surface is found to decrease by 20% every
527 billion years, when considering a rate of mantle cooling of ~100 K/Ga.

528

Supplementary Material:

Water fugacity in the upper mantle

We calculate the water fugacity (f_{H2O}) of pure water based on the previous equation of state (EoS) of H_2O (Pitzer and Sterner, 1994). However, geological fluids/melts are not pure water, at high pressures above ~3 GPa, as they dissolve a significant amount of silicate at high mantle temperatures (Massuyeau et al., 2015; Mibe et al., 2007). It makes the f_{H2O} significantly lower than that of pure H_2O. To take this effect into account, we apply a correction to the f_{H2O} of pure water based on a previous experimental report of the water content of olivine up to 12 GPa and 1673 K (Suppl. Fig. 1) (Bali et al., 2008):

$$f_{H2O} = f_{H2O}^{\text{Pure-water}} *[1 - A_1 \exp(-\Delta G_1/RT)] \qquad \text{(Suppl-Eq. 1)}$$

with ΔG_1 related to the energy of dissolution of the silicate component in the fluid. ΔG_1 can vary with several parameters, in particular temperature and fluid composition. In order to reproduce the ratio of real water fugacity over that of the pure fluid reported previously (Suppl. Fig. 1; (Bali et al., 2008)), we adopted a ΔG_1 value that decreases exponentially with increasing temperature:

$$\Delta G_1 = A_2 \exp(-\Delta G_2/RT) \qquad \text{(Suppl-Eq. 2)}$$

with $A_1=1$, $A_2=2.50 \ 10^{-2}$ and $\Delta G_2=-140$ kJ/mol. For convenience, we use this formalism for further modeling of f_{H2O} in supercritical fluids or hydrous melts at upper mantle pressures and temperatures.
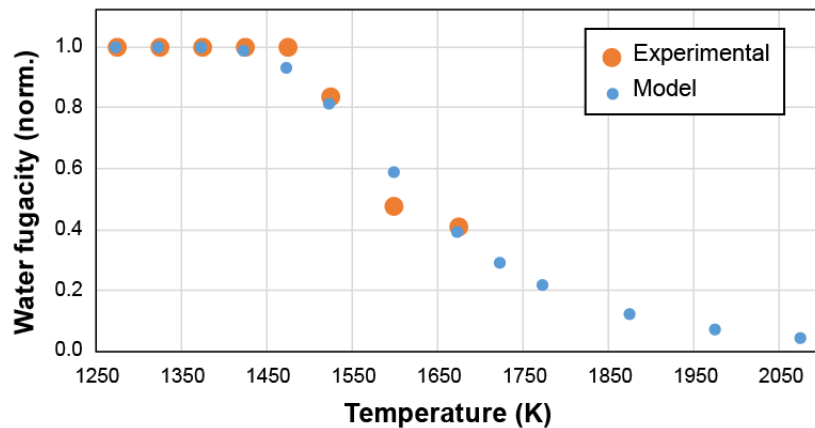
Suppl. Fig. 1: Temperature dependence of water fugacity (i.e. the correction to apply to the f_{H2O} of pure water). Experimental data obtained between 3 and 12 GPa (Bali et al., 2008) are fitted using a double exponential function (Suppl-Eq. 1 and 2). The model reproduces well the amplitude of the f_{H2O} decrease induced by a change of the melt composition (from water-rich to silicate-rich) with increasing the temperature above ~1500 K.

References cited:

Andrault, D., Pesce, G., Manthilake, G., Monteux, J., Bolfan-Casanova, N., Chantel, J., Novella, D., Guignot, N., King, A., Itie, J.-P., Hennet, L., 2018. Deep and persistent melt layer in the Archaean mantle. Nat. Geosci. 11, 139-+.

Ardia, P., Hirschmann, M.M., Withers, A.C., Tenner, T.J., 2012. H_2O storage capacity of olivine at 5-8 GPa and consequences for dehydration partial melting of the upper mantle. Earth Planet. Sci. Lett. 345, 104-116.

Aubaud, C., Hauri, E.H., Hirschmann, M.M., 2004. Hydrogen partition coefficients between nominally anhydrous minerals and basaltic melts. Geophys. Res. Lett. 31.

Bali, E., Bolfan-Casanova, N., Koga, K.T., 2008. Pressure and temperature dependence of H solubility in forsterite : an implication to water activity in the Earth interior. Earth Planet. Sci. Lett., 354-363.

Bercovici, D., Karato, S., 2003. Whole-mantle convection and the transition-zone water filter. Nature 425, 39-44.

Bolfan-Casanova, N., Keppler, H., Rubie, D.C., 2000. Water partitioning between nominally anhydrous minerals in the $MgO-SiO_2-H_2O$ system up to 24 GPa: implications for the distribution of water in the Earth's mantle. Earth Planet. Sci. Lett. 182, 209-221.

Bolfan-Casanova, N., Keppler, H., Rubie, D.C., 2003. Water partitioning at 660 km depth and evidence for very low water solubility in magnesium silicate perovskite. Geophys. Res. Lett. 30, L017182.

Buchen, J., Marquardt, H., Speziale, S., Kawazoe, T., Boffa Ballaran, T., Kurnosov, A., 2018. High-pressure single-crystal elasticity of wadsleyite and the seismic signature of water in the shallow transition zone. Earth Planet. Sci. Lett. 498, 77-87.

Chantel, J., Manthilake, G., Andrault, D., Novella, D., Yu, T., Wang, Y.B., 2016. Experimental evidence supports mantle partial melting in the asthenosphere. Sci. Adv. 2.

Cogne, J.P., Humler, E., 2006. Trends and rhythms in global seafloor generation rate. Geochem., Geophys., Geosyst. 7.

Condamine, P., Frost, D.J., 2018. Kimberlite from incipient melting of the mantle transition zone?, Annual Report of BGI. Bayerisches Geoinstitute, Bareuth.

Courtillot, V., Davaille, A., Besse, J., Stock, J., 2003. Three distinct types of hotspots in the Earth's mantle. Earth Planet. Sci. Lett. 205, 295-308.

Dasgupta, R., Hirschmann, M.M., 2007. A modified iterative sandwich method for determination of near-solidus partial melt compositions. II. Application to determination of near-solidus melt compositions of carbonated peridotite. Contrib. Mineral. Petr. 154, 647-661.

de Leeuw, N.H., Parker, S.C., Catlow, C.R.A., Price, G.D., 2000. Modelling the effect of water on the surface structure and stability of forsterite. Phys. Chem. Mineral. 27, 332-341.

Debayle, E., Bodin, T., Durand, S., Ricard, Y., 2020. Seismic evidence for partial melt below tectonic plates. Nature 586, 555-559.

Debayle, E., Ricard, Y., 2012. A global shear velocity model of the upper mantle from fundamental and higher Rayleigh mode measurements. J. Geophys. Res. 117.

Demouchy, S., 2010. Hydrogen diffusion in spinel grain boundaries and consequences for chemical homogenization in hydrous peridotite. Contrib. Mineral. Petr. 160, 887-898.

Demouchy, S., Shcheka, S., Denis, C.M.M., Thoraval, C., 2017. Subsolidus hydrogen partitioning between nominally anhydrous minerals in garnet-bearing peridotite. Am. Miner. 102, 1822-1831.

Denis, C.M.M., Alard, O., Demouchy, S., 2015. Water content and hydrogen behaviour during metasomatism in the uppermost mantle beneath Ray Pic volcano (Massif Central, France). Lithos 236-237, 256-274.

607 Dong, J., Fischer, R.A., Stixrude, L.P., Lithgow-Bertelloni, C.R., 2021. Constraining the Volume of
608   Earth's Early Oceans With a Temperature-Dependent Mantle Water Storage Capacity Model. AGU
609   Advances 2, e2020AV000323.
610 Doucet, L.S., Peslier, A.H., Ionov, D.A., Brandon, A.D., Golovin, A.V., Goncharov, A.G., Ashchepkov,
611   I.V., 2014. High water contents in the Siberian cratonic mantle linked to metasomatism: An FTIR
612   study of Udachnaya peridotite xenoliths. Geochim. Cosmochim. Acta 137, 159-187.
613 Druzhbin, D., Fei, H., Katsura, T., 2021. Independent hydrogen incorporation in wadsleyite from oxygen
614   fugacity and non-dissociation of H2O in the reducing mantle transition zone. Earth Planet. Sci.
615   Lett. 557, 116755.
616 Durand, S., Debayle, E., Ricard, Y., Zaroli, C., Lambotte, S., 2017. Confirmation of a change in the
617   global shear velocity pattern at around 1000km depth. Geophys. J. Int. 211, 1628-1639.
618 Fei, H., Yamazaki, D., Sakurai, M., Miyajima, N., Ohfuji, H., Katsura, T., Yamamoto, T., 2017. A nearly
619   water-saturated mantle transition zone inferred from mineral viscosity. Sci. Adv. 3.
620 Ferot, A., Bolfan-Casanova, N., 2012. Water storage capacity in olivine and pyroxene to 14 GPa:
621   Implications for the water content of the Earth's upper mantle and nature of seismic discontinuities.
622   Earth Planet. Sci. Lett. 349, 218-230.
623 Flament, N., Coltice, N., Rey, P.F., 2008. A case for late-Archaean continental emergence from thermal
624   evolution models and hypsometry. Earth Planet. Sci. Lett. 275, 326-336.
625 Flament, N., Coltice, N., Rey, P.F., 2013. The evolution of the Sr-87/Sr-86 of marine carbonates does
626   not constrain continental growth. Precambrian Res. 229, 177-188.
627 Freitas, D., Manthilake, G., Chantel, J., Bouhifd, M.A., Andrault, D., 2019. Simultaneous measurements
628   of electrical conductivity and seismicwave velocity of partially molten geological materials: effect
629   of evolving melt texture. Phys. Chem. Mineral. 46, 535-551.
630 Freitas, D., Manthilake, G., Schiavi, F., Chantel, J., Bolfan-Casanova, N., Bouhifd, M.A., Andrault, D.,
631   2017. Experimental evidence supporting a global melt layer at the base of the Earth's upper mantle.
632   Nat. Commun. 8.
633 Frost, D.J., Dolejs, D., 2007. Experimental determination of the effect of H_2O on the 410-km seismic
634   discontinuity. Earth Planet. Sci. Lett. 256, 182-195.
635 Fu, S., Yang, J., Karato, S.-i., Vasiliev, A., Presniakov, M.Y., Gavriliuk, A.G., Ivanova, A.G., Hauri,
636   E.H., Okuchi, T., Purevjav, N., Lin, J.-F., 2019. Water Concentration in Single-Crystal (Al,Fe)-
637   Bearing Bridgmanite Grown From the Hydrous Melt: Implications for Dehydration Melting at the
638   Topmost Lower Mantle. Geophys. Res. Lett. 46, 10346-10357.
639 Fukao, Y., Obayashi, M., 2013. Subducted slabs stagnant above, penetrating through, and trapped below
640   the 660 km discontinuity. J. Geophys. Res. 118, 5920-5938.
641 Gaillard, F., Malki, M., Iacono-Marziano, G., Pichavant, M., Scaillet, B., 2008. Carbonatite Melts and
642   Electrical Conductivity in the Asthenosphere. Science 322, 1363-1365.
643 Green, D.H., Hibberson, W.O., Rosenthal, A., Kovacs, I., Yaxley, G.M., Falloon, T.J., Brink, F., 2014.
644   Experimental Study of the Influence of Water on Melting and Phase Assemblages in the Upper
645   Mantle. Journal of Petrology 55, 2067-2096.
646 Greenwood, R.C., Barrat, J.A., Miller, M.F., Anand, M., Dauphas, N., Franchi, I.A., Sillard, P., Starkey,
647   N.A., 2018. Oxygen isotopic evidence for accretion of Earth's water before a high-energy Moon-
648   forming giant impact. Sci. Adv. 4.
649 Hae, R., Ohtani, E., Kubo, T., Koyama, T., Utada, H., 2006. Hydrogen diffusivity in wadsleyite and
650   water distribution in the mantle transition zone. Earth Planet. Sci. Lett. 243, 141-148.
651 Herzberg, C., Condie, K., Korenaga, J., 2010. Thermal history of the Earth and its petrological
652   expression. Earth Planet. Sci. Lett. 292, 79-88.
653 Hier-Majumder, S., Keel, E.B., Courtier, A.M., 2014. The influence of temperature, bulk composition,
654   and melting on the seismic signature of the low-velocity layer above the transition zone. J. Geophys.
655   Res. 119, 971-983.
656 Hier-Majumder, S., Ricard, Y., Bercovici, D., 2006. Role of grain boundaries in magma migration and
657   storage. Earth Planet. Sci. Lett. 248, 735-749.
658 Hier-Majumder, S., Tauzin, B., 2017. Pervasive upper mantle melting beneath the western US. Earth
659   Planet. Sci. Lett. 463, 25-35.
660 Hirschmann, M.M., 2010. Partial melt in the oceanic low velocity zone. Phys. Earth Planet. Inter. 179,
661   60-71.

662   Hirschmann, M.M., Aubaud, C., Withers, A.C., 2005. Storage capacity of H_2O in nominally anhydrous
663   minerals in the upper mantle. Earth Planet. Sci. Lett. 236, 167-181.
664   Huang, X., Xu, Y., Karato, S., 2005. Water content in the transition zone from electrical conductivity of
665   wadsleyite and ringwoodite. Nature 434, 746-749.
666   Inoue, T., 1994. Effect of water on melting phase relations and melt composition in the system
667   Mg2SiO4□MgSiO3□H2O up to 15 GPa. Phys. Earth Planet. Inter. 85, 237-263.
668   Irifune, T., Isshiki, M., 1998. Iron partitioning in a pyrolite mantle and the nature of the 410-km seismic
669   discontinuity. Nature 392, 702-705.
670   Jing, Z., Karato, S.-i., 2012. Effect of H_2O on the density of silicate melts at high pressures: Static
671   experiments and the application of a modified hard-sphere model of equation of state. Geochim.
672   Cosmochim. Acta 85, 357-372.
673   Katsura, T., Yoneda, A., Yamazaki, D., Yoshino, T., Ito, E., 2010. Adiabatic temperature profile in the
674   mantle. Phys. Earth Planet. Inter. 183, 212-218.
675   Kawakatsu, H., Kumar, P., Takei, Y., Shinohara, M., Kanazawa, T., Araki, E., Suyehiro, K., 2009.
676   Seismic Evidence for Sharp Lithosphere-Asthenosphere Boundaries of Oceanic Plates. Science
677   324, 499-502.
678   Kessel, R., Pettke, T., Fumagalli, P., 2015. Melting of metasomatized peridotite at 4-6 GPa and up to
679   1200 degrees C: an experimental approach. Contrib. Mineral. Petr. 169.
680   Kohlstedt, D.L., Keppler, H., Rubie, D.C., 1996. Solubility of water in the alpha, beta and gamma phases
681   of (Mg,Fe)(2)SiO4. Contrib. Mineral. Petr. 123, 345-357.
682   Kuritani, T., Xia, Q.K., Kimura, J., Liu, J., Shimizu, K., Ushikubo, T., Zhao, D.P., Nakagawa, M.,
683   Yoshimura, S., 2019. Buoyant hydrous mantle plume from the mantle transition zone. Scientific
684   Reports 9.
685   Lambart, S., Laporte, D., Schiano, P., 2009. An experimental study of pyroxenite partial melts at 1 and
686   1.5 GPa: Implications for the major-element composition of Mid-Ocean Ridge Basalts. Earth
687   Planet. Sci. Lett. 288, 335-347.
688   Le Roux, V., Bodinier, J.L., Tommasi, A., Alard, O., Dautria, J.M., Vauchez, A., Riches, A.J.V., 2007.
689   The Lherz spinel lherzolite: Refertilized rather than pristine mantle. Earth Planet. Sci. Lett. 259,
690   599-612.
691   Leahy, G.M., Bercovici, D., 2007. On the dynamics of a hydrous melt layer above the transition zone.
692   J. Geophys. Res. 112.
693   Lecuyer, C., Gillet, P., Robert, F., 1998. The hydrogen isotope composition of seawater and the global
694   water cycle. Chemical Geology 145, 249-261.
695   Liu, Z., Fei, H., Chen, L., McCammon, C., Wang, L., Liu, R., Wang, F., Liu, B., Katsura, T., 2021.
696   Bridgmanite is nearly dry at the top of the lower mantle. Earth Planet. Sci. Lett. 570, 117088.
697   Liu, Z., Park, J., Karato, S.-i., 2016. Seismological detection of low-velocity anomalies surrounding the
698   mantle transition zone in Japan subduction zone. Geophys. Res. Lett. 43, 2480-2487.
699   Liu, Z., Park, J., Karato, S.-i., 2018. Seismic evidence for water transport out of the mantle transition
700   zone beneath the European Alps. Earth Planet. Sci. Lett. 482, 93-104.
701   Machida, S., Kogiso, T., Hirano, N., 2017. Petit-spot as definitive evidence for partial melting in the
702   asthenosphere caused by CO2. Nat. Commun. 8.
703   Mao, Z., Jacobsen, S.D., Jiang, F., Smyth, J.R., Holl, C.M., Duffy, T.S., 2008. Elasticity of hydrous
704   wadsleyite to 12 GPa: Implications for Earth's transition zone. Geophys. Res. Lett. 35.
705   Marty, B., 2012. The origins and concentrations of water, carbon, nitrogen and noble gases on Earth.
706   Earth Planet. Sci. Lett. 313, 56-66.
707   Massuyeau, M., Gardés, E., Morizet, Y., Gaillard, F., 2015. A model for the activity of silica along the
708   carbonatite-kimberlite-mellilitite-basanite melt compositional joint. Chemical Geology 418, 206-
709   216.
710   Matsukage, K.N., Jing, Z.C., Karato, S., 2005. Density of hydrous silicate melt at the conditions of
711   Earth's deep upper mantle. Nature 438, 488-491.
712   Mibe, K., Kanzaki, M., Kawamoto, T., Matsukage, K.N., Fei, Y.W., Ono, S., 2007. Second critical
713   endpoint in the peridotite-H2O system. J. Geophys. Res. 112.
714   Mibe, K., Orihashi, Y., Nakai, S., Fujii, T., 2006. Element partitioning between transition-zone minerals
715   and ultramafic melt under hydrous conditions. Geophys. Res. Lett. 33.

716   Michael, P.J., 1988. The concentration, behavior and storage of H2O in the suboceanic upper mantle:
717   Implications for mantle metasomatism. Geochim. Cosmochim. Acta 52, 555-566.
718   Mierdel, K., Keppler, H., Smyth, J.R., Langenhorst, F., 2007. Water solubility in aluminous
719   orthopyroxene and the origin of Earth's asthenosphere. Science 315, 364-368.
720   Mosenfelder, J.L., Deligne, N.I., Asimow, P.D., Rossman, G.R., 2006. Hydrogen incorporation in
721   olivine from 2-12 GPa. Am. Miner. 91, 285-294.
722   Ni, H., Keppler, H., Behrens, H., 2011. Electrical conductivity of hydrous basaltic melts: implications
723   for partial melting in the upper mantle. Contrib. Mineral. Petr. 162, 637-650.
724   Nishi, M., Irifune, T., Tsuchiya, J., Tange, Y., Nishihara, Y., Fujino, K., Higo, Y., 2014. Stability of
725   hydrous silicate at high pressures and water transport to the deep lower mantle. Nat. Geosci. 7, 224-
726   227.
727   Novella, D., Frost, D.J., Hauri, E.H., Bureau, H., Raepsaet, C., Roberge, M., 2014. The distribution of
728   H_2O between silicate melt and nominally anhydrous peridotite and the onset of hydrous melting in
729   the deep upper mantle. Earth Planet. Sci. Lett. 400, 1-13.
730   O'Reilly, S.Y., Griffin, W.L., 2013. Mantle metasomatism. Metasomatism and the Chemical
731   Transformation of Rock, Lecture Notes in Earth System Sciences. Springer Berlin Heidelberg, pp.
732   471-533.
733   Ohtani, E., Mizobata, H., Yurimoto, H., 2000. Stability of dense hydrous magnesium silicate phases in
734   the systems Mg_2SiO_4-H_2O and $MgSiO_3$-
735   H_2O at pressures up to 27 GPa. Phys. Chem. Mineral. 27, 533-544.
736   Ohtani, E., Yuan, L., Ohira, I., Shatskiy, A., Litasov, K., 2018. Fate of water transported into the deep
737   mantle by slab subduction. Journal of Asian Earth Sciences 167, 2-10.
738   Padrón-Navarta, J.A., Hermann, J., 2017. A Subsolidus Olivine Water Solubility Equation for the Earth's
739   Upper Mantle. J. Geophys. Res. 122, 9862-9880.
740   Pamato, M.G., Myhill, R., Ballaran, T.B., Frost, D.J., Heidelbach, F., Miyajima, N., 2015. Lower-mantle
741   water reservoir implied by the extreme stability of a hydrous aluminosilicate. Nat. Geosci. 8, 75-
742   79.
743   Pearson, D.G., Brenker, F.E., Nestola, F., McNeill, J., Nasdala, L., Hutchison, M.T., Matveev, S.,
744   Mather, K., Silversmit, G., Schmitz, S., Vekemans, B., Vincze, L., 2014. Hydrous mantle transition
745   zone indicated by ringwoodite included within diamond. Nature 507, 221-+.
746   Piani, L., Marrocchi, Y., Rigaudier, T., Vacher, L.G., Thomassin, D., Marty, B., 2020. Earth's water
747   may have been inherited from material similar to enstatite chondrite meteorites. Science 369, 1110-
748   +.
749   Pitzer, K.S., Sterner, S.M., 1994. Equation of state valid continuously from zero to extreme pressures
750   for H_2O and CO_2. J. Chem. Phys. 101, 3111-3116.
751   Pope, E.C., Bird, D.K., Rosing, M.T., 2012. Isotope composition and volume of Earth's early oceans.
752   Proc. Natl. Acad. Sci. U. S. A. 109, 4371-4376.
753   Priestley, K., McKenzie, D., 2013. The relationship between shear wave velocity, temperature,
754   attenuation and viscosity in the shallow part of the mantle. Earth Planet. Sci. Lett. 381, 78-91.
755   Revenaugh, J., Jordan, T.H., 1991. Mantle layering from SCS reverberations 3. The upper mantle. J.
756   Geophys. Res. 96, 19781-19810.
757   Revenaugh, J., Sipkin, S.A., 1994. Seismic evidence for silicate melt atop the 410 km mantle
758   discontinuity. Nature 369, 474-476.
759   Rupke, L.H., Morgan, J.P., Hort, M., Connolly, J.A.D., 2004. Serpentine and the subduction zone water
760   cycle. Earth Planet. Sci. Lett. 223, 17-34.
761   Sakamaki, T., Suzuki, A., Ohtani, E., 2006. Stability of hydrous melt at the base of the Earth's upper
762   mantle. Nature 439, 192-194.
763   Sarafian, E., Gaetani, G.A., Hauri, E.H., Sarafian, A.R., 2017. Experimental constraints on the damp
764   peridotite solidus and oceanic mantle potential temperature. Science 355, 942-944.
765   Schmandt, B., Jacobsen, S.D., Becker, T.W., Liu, Z.X., Dueker, K.G., 2014. Dehydration melting at the
766   top of the lower mantle. Science 344, 1265-1268.
767   Shirey, S.B., Wagner, L.S., Walter, M.J., Pearson, D.G., van Keken, P.E., 2021. Slab Transport of Fluids
768   to Deep Focus Earthquake Depths—Thermal Modeling Constraints and Evidence From Diamonds.
769   AGU Advances 2, e2020AV000304.

770 Smyth, J.R., Frost, D.J., Nestola, F., Holl, C.M., Bromiley, G., 2006. Olivine hydration in the deep upper
771   mantle: Effects of temperature and silica activity. Geophys. Res. Lett. 33.
772 Soltanmohammadi, A., Gregoire, M., Rabinowicz, M., Gerbault, M., Ceuleneer, G., Rahgoshay, M.,
773   Bystricky, M., Benoit, M., 2018. Transport of Volatile-rich Melt from the Mantle Transition Zone
774   via Compaction Pockets: Implications for Mantle Metasomatism and the Origin of Alkaline Lavas
775   in the Turkish-Iranian Plateau. Journal of Petrology 59, 2273-2309.
776 Song, T.R.A., Helmberger, D.V., Grand, S.P., 2004. Low-velocity zone atop the 410-km seismic
777   discontinuity in the northwestern United States. Nature 427, 530-533.
778 Stagno, V., Ojwang, D.O., McCammon, C.A., Frost, D.J., 2013. The oxidation state of the mantle and
779   the extraction of carbon from Earth's interior. Nature 493, 84-88.
780 Swain, M.V., Atkinson, B.K., 1978. Fracture surface-energy of olivine. Pure and Applied Geophysics
781   116, 866-872.
782 Tauzin, B., Debayle, E., Wittlinger, G., 2010. Seismic evidence for a global low-velocity layer within
783   the Earth's upper mantle. Nat. Geosci. 3, 718-721.
784 Toffelmier, D.A., Tyburczy, J.A., 2007. Electromagnetic detection of a 410-km-deep melt layer in the
785   southwestern United States. Nature 447, 991-994.
786 Toplis, M.J., 2005. The thermodynamics of iron and magnesium partitioning between olivine and liquid:
787   criteria for assessing and predicting equilibrium in natural and experimental systems. Contrib.
788   Mineral. Petr. 149, 22-39.
789 van Keken, P.E., Hacker, B.R., Syracuse, E.M., Abers, G.A., 2011. Subduction factory: 4. Depth-
790   dependent flux of H_2O from subducting slabs worldwide. J. Geophys. Res. 116.
791 Vinnik, L., Farra, V., 2007. Low S velocity atop the 410-km discontinuity and mantle plumes. Earth
792   Planet. Sci. Lett. 262, 398-412.
793 Wang, X.-C., Wilde, S.A., Li, Q.-L., Yang, Y.-N., 2015. Continental flood basalts derived from the
794   hydrous mantle transition zone. Nat. Commun. 6, 7700.
795 Wen, L.X., Anderson, D.L., 1995. The fate of slabs inferred from seismic tomography and 130 million
796   years of subduction. Earth Planet. Sci. Lett. 133, 185-198.
797 Xiao, J., Hier-Majumder, S., Tauzin, B., Waltham, D., 2020. An inversion approach for analysing the
798   physical properties of a seismic low-velocity layer in the upper mantle. Phys. Earth Planet. Inter.
799   304.
800 Yang, X., 2016. Effect of oxygen fugacity on OH dissolution in olivine under peridotite-saturated
801   conditions: An experimental study at 1.5–7GPa and 1100–1300°C. Geochim. Cosmochim. Acta
802   173, 319-336.
803 Yoshino, T., Manthilake, G., Matsuzaki, T., Katsura, T., 2008. Dry mantle transition zone inferred from
804   the conductivity of wadsleyite and ringwoodite. Nature 451, 326-329.
805 Yoshino, T., Nishihara, Y., Karato, S., 2007. Complete wetting of olivine grain boundaries by a hydrous
806   melt near the mantle transition zone. Earth Planet. Sci. Lett. 256, 466-472.
807 Zhang, Z., Dueker, K.G., Huang, H.-H., 2018. Ps mantle transition zone imaging beneath the Colorado
808   Rocky Mountains: Evidence for an upwelling hydrous mantle. Earth Planet. Sci. Lett. 492, 197-
809   205.
810 Zhao, Y.H., Ginsberg, S.B., Kohstedt, D.L., 2004. Solubility of hydrogen in olivine: dependence on
811   temperature and iron content. Contrib. Mineral. Petr. 147, 155-161.
812